RSC Advances

PAPER

View Article Online
View Journal | View Issue

Cite this: *RSC Adv.*, 2022, **12**, 14007

Realizing outstanding electrochemical performance with $Na_3V_2(PO_4)_2F_3$ modified with an ionic liquid for sodium-ion batteries†

Xiaobo Yu, Tianyi Lu, Xiaokai Li, Jiawei Qi, Luchen Yuan, Zu Man and Haitao Zhuo *

Received 28th February 2022
Accepted 1st May 2022

DOI: 10.1039/d2ra01292h

rsc.li/rsc-advances

$Na_3V_2(PO_4)_2F_3$ is a typical NASICON structure with a high voltage plateau and capacity. Nevertheless, its applications are limited due to its low conductivity and poor rate performance. In this study, nitrogen–boron co-doped carbon-coated $Na_3V_2(PO_4)_2F_3$ (NVPF-CNB) was prepared by a simple sol–gel method using an ionic liquid (1-vinyl-3-methyl imidazole tetrafluoroborate) as a source of nitrogen and boron for the first time. The morphology and electrochemical properties of NVPF-CNB composites were investigated. The results show that a nitrogen–boron co-doped carbon layer could increase the electron and ion diffusion rate, reduce internal resistance, and help alleviate particle agglomeration. NVPF-CNB-30 exhibited better rate performance under 5C and 10C charge/discharge with initial reversible capacities of 99 and 90 mA h g^{-1}, respectively. Furthermore, NVPF-CNB-30 illustrates excellent cyclic performance with the capacity retention rate reaching 91.9% after 500 cycles at 5C, as well as a capacity retention rate of about 95.5% after 730 cycles at 10C. The evolution of the material's structure during charge/discharge processes studied by *in situ* X-ray diffraction confirms the stable structure of nitrogen–boron co-doped carbon-coated $Na_3V_2(PO_4)_2F_3$. Co-doping of nitrogen and boron also provides more active sites on the surface of $Na_3V_2(PO_4)_2F_3$, revealing a new strategy for the modification of sodium-ion batteries.

1. Introduction

With the rapid increase in population and economic growth and technological advancement at the global scale, consumption of energy has increased tremendously. At present, most of the energy is produced from fossil fuels;[1] nonetheless, fossil fuels are non-renewable energy sources and have a greater impact on the environment, thus the development of new energy sources is imminent.[2,3] As a new source of secondary energy, lithium-ion batteries (LIBs) are beneficial and used in various electronics, electric vehicles, and large-scale equipment. However, with the increase in demand for LIBs, their price continues to soar high. Moreover, the distribution of lithium in the earth's crust is non-uniform and very limited; thus, the supply of lithium could be short in the future.[4,5] Therefore, it is of great significance to find alternatives to LIBs. Notably, the physical and chemical properties of sodium, are very similar to those of lithium.[6,7] Therefore, sodium-ion batteries have received significant research attention and are considered promising candidates to replace LIBs. Sodium-ion batteries have the following advantages: (1) sodium is rich in reserves and low in price.[8] (2) For the same concentration of electrolyte, the conductivity of sodium electrolyte is higher than that of lithium electrolyte, thus sodium ion battery can use low concentration electrolyte.[9] (3) Sodium ions do not form alloys with aluminum; therefore, aluminum can be used as the current collector in sodium-ion batteries.[10] However, the radius of sodium ions is larger than that of lithium ions, and it occupies a larger volume and exhibits lower electrochemical performance in sodium-ion batteries.[11] The current research on sodium-ion cathode materials mainly includes layered transition metal ion oxides,[12–14] Prussian blue analogs,[15,16] and polyanionic compounds.[17,18] Among them, the polyanionic compounds have tetrahedral or octahedral structural units, connected *via* covalent bonds to form a stable three-dimensional (3D) network structure.[19] For example, $NaFePO_4$,[20,21] $Na_3V_2(PO_4)_3$,[22–24] $Na_3V_2(PO_4)_2F_3$,[25,26] $NaVPO_4F$[27,28] all exhibit good electrochemical performance. Among these, $Na_3V_2(PO_4)_2F_3$ (NVPF) exhibits a higher working voltage due to the induction effect of F^-, and the theoretical specific capacity reaches up to 128 mA h g^{-1}. Besides, the open 3D structure is more conducive to the free diffusion of sodium ions.[29]

However, its low intrinsic conductivity affects the electrochemical performance. To overcome this problem, various methods such as carbon coating,[30–32] morphological changes,[33,34] element doping,[35] and particle size tuning[36,37] have been mainly used. Among them, the doping of heteroatoms

College of Chemistry and Environmental Engineering, Shenzhen University, Shenzhen, 518060, P. R. China. E-mail: haitaozhuo@163.com

† Electronic supplementary information (ESI) available. See https://doi.org/10.1039/d2ra01292h

such as nitrogen, boron, sulfur, and phosphorus in the carbon layer has been extensively used. Nitrogen (N) is the most widely used heteroatom in doping of cathode materials to improve the active sites and wettability of the material surface, which thus improves the battery performance.[38–40] For example, Li *et al.* improved the conductivity of sodium ions by applying N-doped carbon NVPF composite.[41] The composite material promoted the transmission of sodium ions and demonstrated the reversible capacity of 109.5 mA h g^{-1} at 0.1C. Compared with the single atom doped carbon layer, the double atom doped carbon layer can generate more active sites, enhance the diffusion of sodium ions and improve the battery performance.[42,43] Huang *et al.*[44] successfully prepared nitrogen–sulfur co-doped carbon $Na_3V_2(PO_4)_3$ (NVP-C-NS) *via* a simple sol–gel method. After 500 cycles of NVP-C-NS at 200 A g^{-1}, the discharge capacity of NVP-C-NS is 74.2 mA h g^{-1}, and the capacity retention rate reached 83.4%. Boron doping is also an effective modification approach to improve battery performance.[45] Yu *et al.* successfully synthesized nitrogen–boron co-doped carbon-coated $Na_3V_2(PO_4)_3$ composite,[46] which maintained a high discharge capacity of 79 mA h g^{-1} after 2000 cycles at 100C. Ionic liquids consist of ions composed of organic cations and inorganic or organic anions, with low volatility, a characteristic suitable for environmental protection and sustainable development. Moreover, ionic liquids offer other advantages such as low viscosity, better wettability, and good fluidity, which make them conducive to the formation of uniform coatings materials surface.[47,48] Owing to these characteristics, ionic liquids appear as a unique synthesis medium, and by using them, materials with specific morphologies and properties can be obtained, which cannot be achieved using traditional solvents. Ionic liquids are also used as carbon sources in electrode materials.[49–52]

In this study, nitrogen–boron co-doped carbon-coated $Na_3V_2(PO_4)_2F_3$ (NVPF-CNB) was synthesized using 1-vinyl-3-methyl imidazole tetrafluoroborate as nitrogen and boron source. Moreover, the effect of ionic liquid dosage on NVPF was investigated. Among different combinations, NVPF-CNB-30 exhibited excellent initial capacity 99 and 90 mA h g^{-1} at 5C and 10C, respectively, and excellent cycle stability (capacity retention rate was about 95.5% after 730 cycles at 10C). Non-metallic heteroatom doping enhances the active sites, facilitates the diffusion and electron transport of sodium ions, and improves the electrical conductivity of materials.

2. Experimental

2.1. Synthesis of NVPF-CNB

Fig. 1 exhibits that NVPF-CNB composite was synthesized by sol–gel method, using NaF, NH_4VO_3, $NH_4H_2PO_4$, and citric acid as raw materials, and citric acid as a chelating agent and carbon source. First, NH_4VO_3 (AR, 0.01 mol), citric acid (AR, 0.008 mol), NaF (AR, 0.015 mol), and $NH_4H_2PO_4$ (AR, 0.01 mol) were sequentially dissolved in deionized water, heated at 60 °C, and stirred continuously for 2 h to form a uniform solution. Then different amounts of ionic liquid (1-vinyl-3-methyl imidazole tetrafluoroborate) were added to the reaction mixture and the contents were continuously stirred at 60 °C to obtain a gel. Subsequently, the gel was dried in a freeze dryer, ground in an agate mortar, and transferred to a tube furnace for pre-sintering at 350 °C for 4 h under argon atmosphere. Then the obtained powder was ground again and heat-treated at 650 °C for 10 h under argon atmosphere. The composite materials were labeled as NVPF-C, NVPF-CNB-20, NVPF-CNB-30, and NVPF-CNB-40 according to the amount of ionic liquid added (0, 20, 30, and 40% of NVPF mass, respectively).

2.2. Materials characterization

The crystallinity of samples was determined by X-ray diffraction (XRD) in the scanning range of 10 to 80° (Malvern Panalytical Empyrean, Netherlands). The carbon content of composites was analyzed by thermogravimetric analysis (TGA, METTLER TGA/DSC 3+) in an air atmosphere between 25 and 800 °C. The carbon phase of materials was analyzed by Raman spectroscopy (Renishaw in Via Raman Microscope, UK). Fourier transform spectroscopy (FT-IR) using a tableting method and ATR mold was used to identify substances and analyze their structures (Shimadzu IRAffinity-1, Japan). Field-emission scanning electron microscopy (FE-SEM) and energy dispersive X-ray

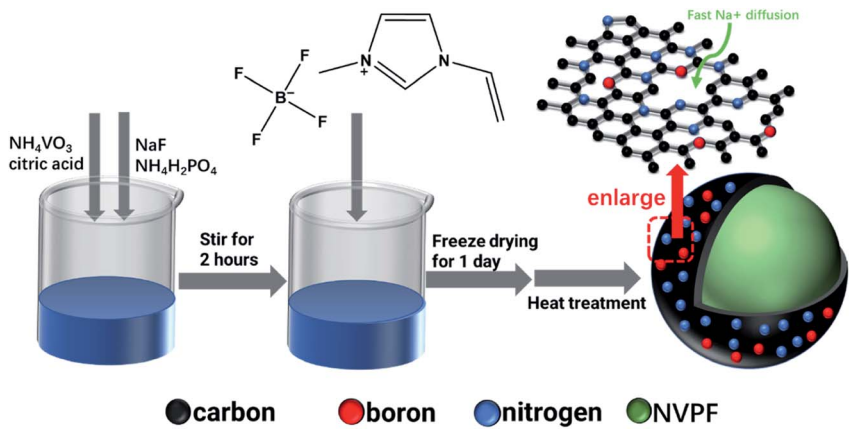

Fig. 1 Schematic illustration of the fabrication process of NVPF-CNB.

spectroscopy (EDS, JEOL JSM-7800F and TEAM Octane Plus) were used to characterize the morphology and elemental distribution of composites. Nitrogen adsorption and desorption isotherms were measured using specific surface area and porosity analyzer (Gemini V2380, US). Transmission electron microscopy (TEM, JEM-2100 & X-MAX80) was used to investigate the inner morphology of composites. The surface composition of materials was analyzed by X-ray photoelectron spectroscopy (Thermo Fisher Scientific K-Alpha+).

For *in situ* XRD experiments, a special cell employing aluminum foil as current collector and testing window was assembled to monitor the *in situ* reactions during cycling. The *in situ* charge/discharge processes of the batteries were continuously performed without intervals between scans. The scan speed of the *in situ* XRD test was 8° per minute, and the scan range was 10° to 40°, and the charge/discharge current was 64 mA g^{-1}.

2.3. Electrochemical characterization

To test the electrochemical performance of samples, a button cell was assembled in a glove box filled with argon. The positive electrode materials, acetylene black, and binder polyvinylidene fluoride were mixed in a mass ratio of 8 : 1 : 1 and dispersed in 1-methyl-2-pyrrolidone (NMP) solution. The black viscous slurry was stirred at a uniform speed for 15 min in a stirring defoam machine (A-310, China). The slurry was spread on the aluminum foil and dried in a blast dryer for 6 h. The mass loading of active material was about 2.5 mg cm^{-2}. NVPF-CNB was used as the working electrode, sodium tablet as the counter electrode, $NaClO_4$ (1 mol L^{-1}) in propylene carbonate (PC) with fluoroethylene carbonate (FEC, 5.0%) as the electrolyte, and glass fiber (Whatman, GF/D) as the diaphragm. The obtained coin cells were tested using a Neware multichannel battery test system in the voltage range of 2.0–4.3 V. Cyclic voltammetry (CV) tests were performed on an electrochemical workstation (Solartron Analytical 1400) at different scanning rates in the voltage range of 2.5–4.5 V. The electrochemical impedance spectroscopy (EIS) testes were carried out in the frequency range of 0.01–100 kHz.

3. Results and discussion

The XRD patterns of all NVPF composites are shown in Fig. 2a. All the diffraction peaks of NVPF with different amounts of ionic liquid (0, 20, 30, and 40%) correspond to the standard diffraction peaks of $Na_3V_2(PO_4)_2F_3$(PDF# 89-8485). There is no carbon diffraction peak around 26.5°, indicating that carbon may exist in an amorphous form.[53] Fig. 2b, exhibits that the XRD data of NVPF-CNB-30 were refined by Rietveld method, indicating that the adopted modification method has little effect on the crystal structure of the material. The unit cell parameters of the NVPF-CNB-30 sample were calculated as $a = b = 9.043$ Å, $c = 10.748$ Å, and $V = 879.1153$ Å. It belongs to the tetragonal system and the space group is $P4_2/mnm$. This is consistent with the results of related previous reports.[54,55] Fig. 2c shows the Fourier transform infrared (FT-IR) spectra of NVPF-CNB-30, NVPF-CNB-20, NVPF-CNB-40, and NVPF-C. In the FT-IR spectrum, the wide-band at 1040–1140 cm^{-1} is attributed to the anti-symmetric stretching of the PO_4 tetrahedral structure. Peaks at 550 and 680 cm^{-1} represent the P–O bond in the material. The band at 920 cm^{-1} is attributed to the V–O bond in the VO_4F_2. There is no significant difference in FT-IR spectra of the four samples with different ionic liquid content. Raman spectroscopy results confirm the presence of carbon in the material. Fig. S1,† demonstrates that NVPF-CNB-30, NVPF-CNB-20, NVPF-CNB-40 and NVPF-C samples show two different

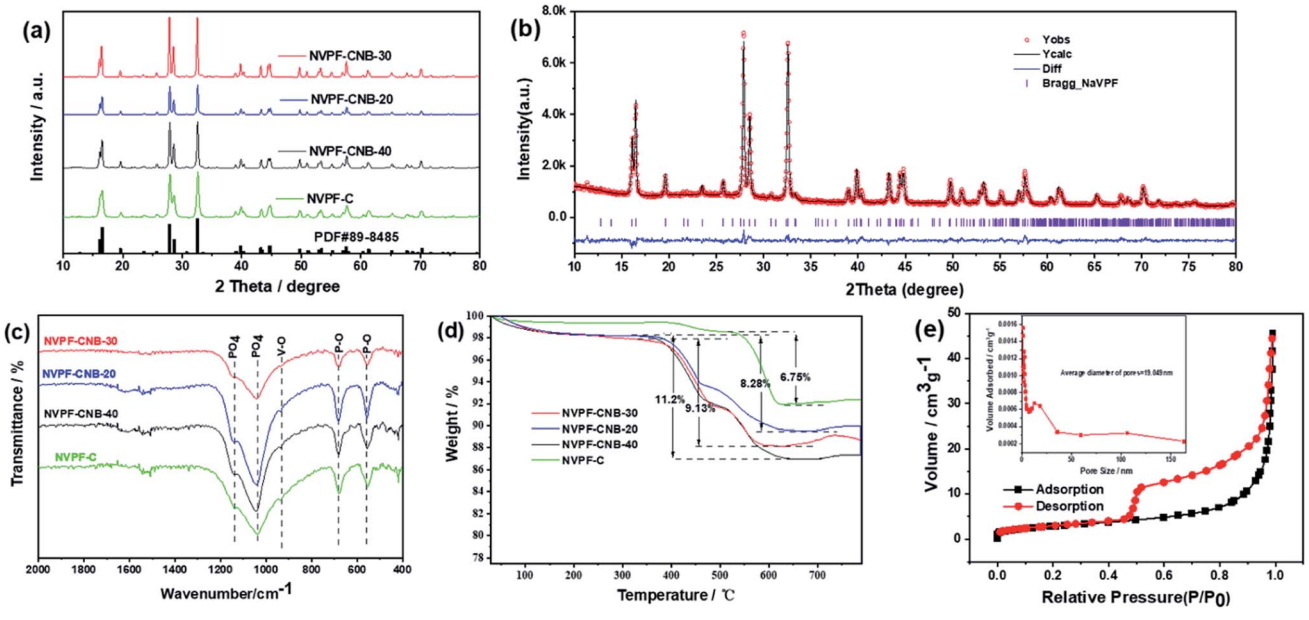

Fig. 2 (a) XRD patterns of all samples, (b) the Rietveld-refined XRD patterns of NVPF-CNB-30, (c) FT-IR spectra of all samples, (d) TGA curves of all samples, (e) N_2 adsorption–desorption isotherms, and corresponding BJH pore-size distribution curve (the inset) of NVPF-CNB-30.

peaks at 1355 and 1597 cm^{-1}, attributed to the D-band (sp^2-type carbon) and the G-band (sp^3-type carbon), respectively.[56] The peak intensity ratio of the D-band to the G-band (I_D/I_G) indicates the degree of disorder and defect quantity in graphitic carbon.[57] The I_D/I_G peak intensity ratio is 0.91 for NVPF-CNB-30, 0.90 for NVPF-CNB-40, 0.90 for NVPF-CNB-20 and 0.89 for NVPF-C. The I_D/I_G value of NVPF-CNB-30 is slightly greater than that of NVPF-C. It shows that the nitrogen and boron co-doped carbon layer of NVPF-CNB-30 produces more defects, is beneficial to the diffusion of sodium ions, and improves electrochemical performance. In order to measure the carbon content of the samples, TGA was performed. TGA curve shows the loss of the relative mass in the sample (Fig. 2d). Initially, due to the evaporation of adsorbed water, curves drop slightly,[58] and the curve rises slightly beyond 600 °C due to V^{3+} reduction.[59] Based on this, result and from the weight loss stage between 350 and 600 °C, the contents of carbon in NVPF-C, NVPF-CNB-20, NVPF-CNB-30, and NVPF-CNB-40 are approximately 6.75, 8.28, 9.13, and 11.2 wt%, respectively. To explore the pore size distribution and specific surface area of NVPF-CNB composite, N_2 isothermal-adsorption technique was employed. Fig. 2e shows that NVPF-CNB-30 exhibits type-IV isothermal adsorption–desorption curves.[60] The Barrett–Joyner–Halenda (BJH) pore size distribution curve (inset of Fig. 2e) reveals that the pore diameter of NVPF-CNB-30 is distributed around 2–35 nm, and it has mesoporous structure.[61] The distribution of mesopores could contribute to inhibiting the agglomeration of the material.[62] The specific surface area calculated according to the Brunauer–Emmett–Teller (BET) model for NVPF-CNB-30 is 45 $m^2\ g^{-1}$. This high surface area facilitates the penetration of electrolyte and also the contact between the active material and the electrolyte.[63]

The valence states and elements present in NVPF-CNB-30 were analyzed by XPS. Fig. S2† illustrates that in addition to the actual elemental composition of NVPF, elements such as C, N, and B are also present in the sample, confirming the successful doping of N and B in NVPF. Fig. 3a, exhibits that the narrow spectrum of C 1s is fitted to three peaks at 284.6, 285.5 and 289.6 eV corresponding to C=C bond; C–O, or C–O–B or C–N bond; and O–C=O or O=C–N bond, respectively. Moreover, the narrow spectrum of N 1s is fitted to three peaks at 398.2, 399.1, and 401.0 eV corresponding to pyridine nitrogen, pyrrole nitrogen, and graphite nitrogen, respectively (Fig. 3b). Notably, the presence of pyridine N and graphite N can improve electrochemical performance, in particular, rate performance and conductivity.[64,65] Whereas, the narrow spectrum of B 1s is fitted to five peaks of 192.2, 191.2, 190.0, 189.1, and 188.2 eV corresponding to BCO_2, BC_2O, N–B bond, BC_3, and B_4C, respectively (Fig. 3c). The presence of BC_3 improves the electronic conductivity of the carbon layer.[66] The fitting results of C 1s and B 1s further indicate the successful doping of N and B, resulting in more defects and active sites in the carbon layer, promoting the diffusion of sodium ions, and improving the electrochemical properties of the material.

Fig. 4e shows an electron micrograph of NVPF-CNB-30 obtained by SEM, revealing the porous morphology of the composite. Moreover, NVPF-C and NVPF-CNB composites were observed at the same magnification (Fig. 4a–d). Obviously, NVPF-CNB-30 consists of finer particles, and the particle size distribution is more uniform. Compared with NVPF-C, less agglomeration is observed in NVPF-CNB composite. This is attributed to the fact that the CBN framework prevents the growth of particles during the sintering process, and the smaller particle size is also conducive to the wetting of the electrolyte, thus leading to the improvement in the electrochemical performance of composite. To demonstrate the distribution of carbon layer in the internal structure of particles, TEM images were obtained, as shown in Fig. 4f–h. Fig. 4f shows that the particles are porous and coated with a carbon layer. Fig. 4g and h show that the thickness of carbon coating is in the range of 5–10 nm. These carbon layers limit the material growth during the sintering process and increase the electrical conductivity. Moreover, the lattice fringes of the material, with lattice spacing of 0.3455 and 0.3771 nm respectively, can be seen inside the carbon coating. These results are consistent with the (202) and (211) crystal planes of NVPF, further revealing the high crystallinity of NVPF-CNB-30. Fig. 5 shows the EDS element analysis of the NVPF-CNB-30 composite where C, N, B, O, Na, P, and V are uniformly dispersed in the material, confirming the existence of N and B. For comparative analysis, the morphologies of the newly fabricated and cycled NVPF-CNB-30 cathodes were characterized by SEM. Fig. S3† presents that the NVPF-CNB-30 cathode surface before cycling exhibits uniform morphology

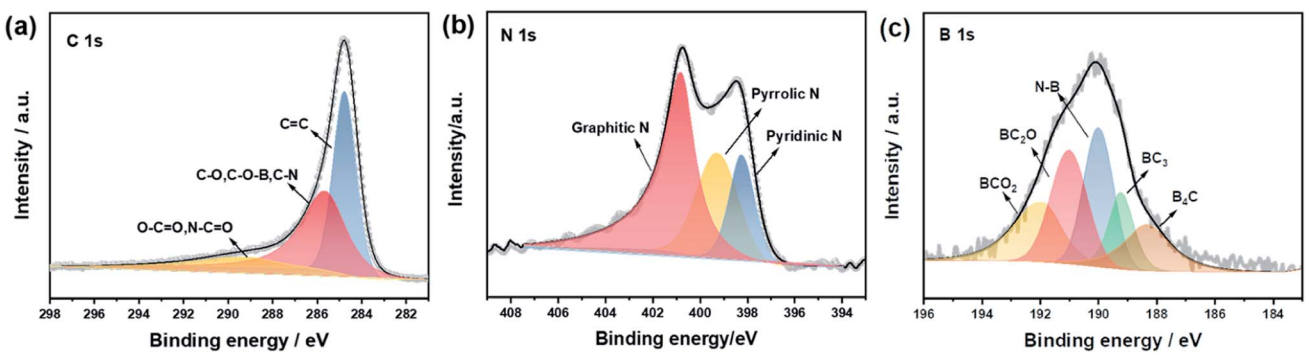

Fig. 3 High-resolution XPS spectra of NVPF-CNB-30: (a) C 1s, (b) N 1s and (c) B 1s.

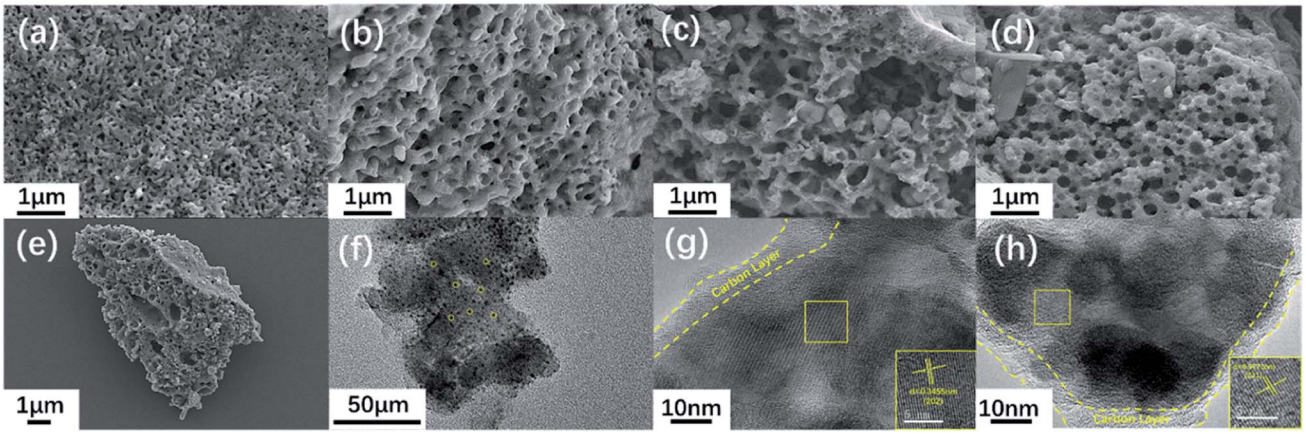

Fig. 4 (a–e) SEM images of all samples: (a) NVPF-CNB-30, (b) NVPF-CNB-20, (c) NVPF-CNB-40, (d) NVPF-C, (e) NVPF-CNB-30; (f–h) TEM images of NVPF-CNB-30 composite.

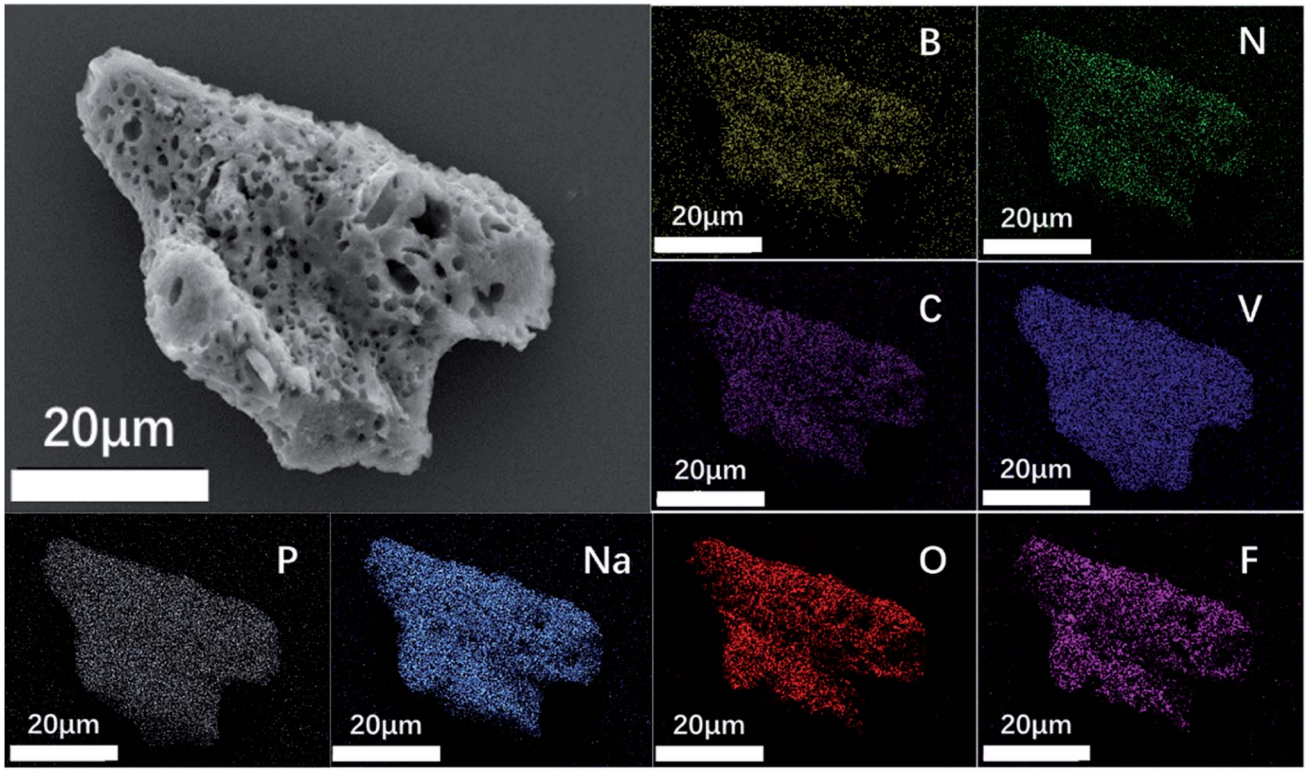

Fig. 5 EDS elemental mapping of NVPF-CNB-30 composite.

and integrity. NVPF-CNB-30 cathode still maintains its intact structure even after 730 cycles.

To investigate the structure of NVPF-CNB-30, *in situ* XRD analysis was carried out during charging and discharging. Fig. 6 shows the XRD spectrum of NVPF-CNB-30 at different voltages. When NVPF-CNB-30 is charged from its open-circuit voltage to 3.7 V, the (220) and (222) crystal planes of NVPF shift toward higher angles due to the transformation of $Na_3V_2(PO_4)_2F_3$ to $Na_2V_2(PO_4)_2F_3$ and the extraction of Na^+. When the voltage reaches 4.2 V, the (220) and (222) crystal planes of the NVPF continue to shifted toward high angles, which is attributed to the transformation of $Na_2V_2(PO_4)_2F_3$ to $Na_1V_2(PO_4)_2F_3$, at the same time, another Na^+ is extracted.[67,68] During discharging process, the (220) and (222) crystal planes of NVPF deviate toward low angles. After two complete charging and discharging cycle, the peak positions of all the crystal planes return to the original state, indicating excellent reversibility of NVPF-CNB-30.

The prepared NVPF samples were coated with different amounts of ionic liquid as the cathode material for sodium ion batteries for electrochemical performance tests. Fig. 7a shows

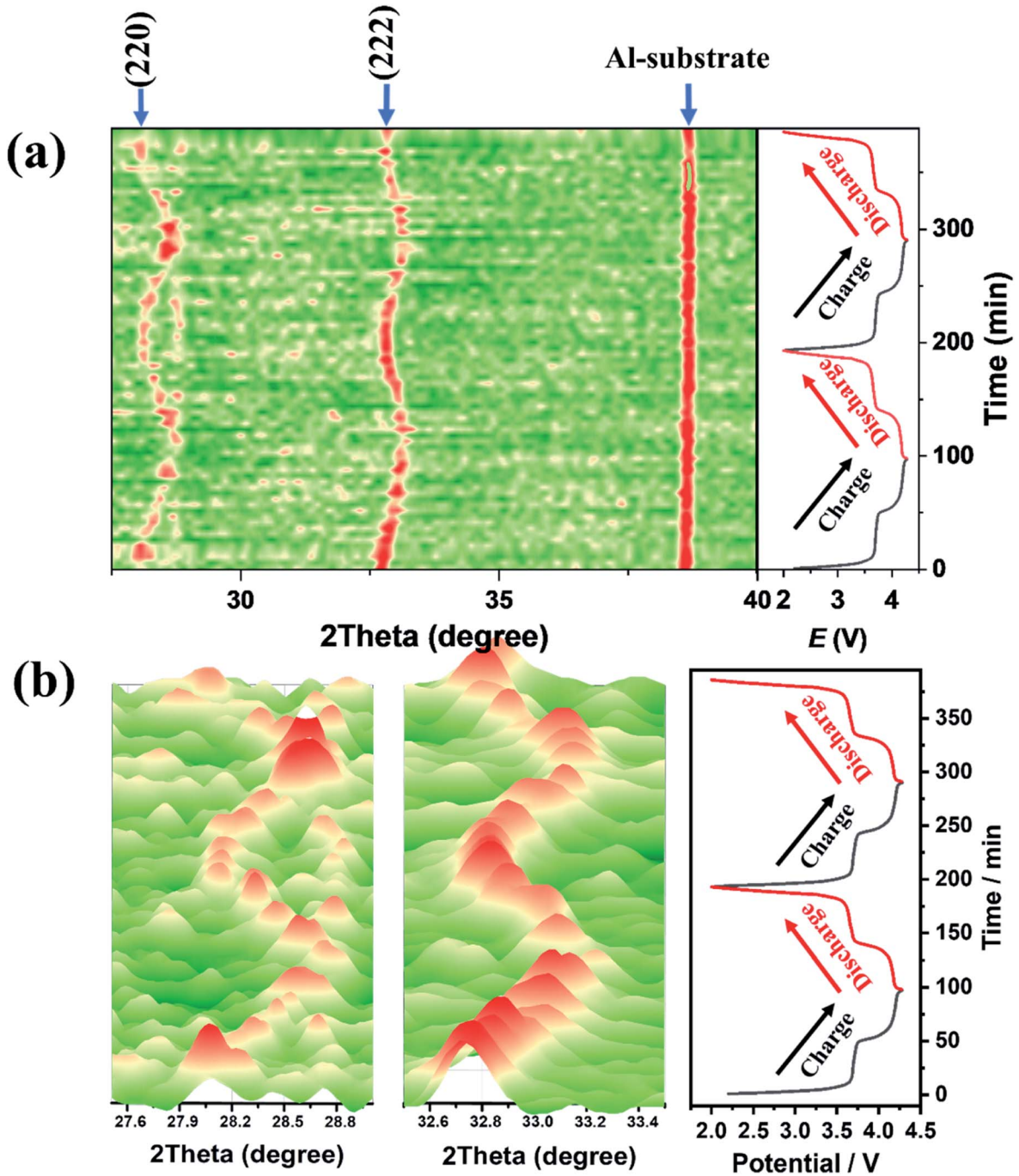

Fig. 6 (a) *In situ* XRD patterns of NVPF-CNB-30 under different conditions. (b) The partially enlarged XRD patterns at 27.5–28.9° and 32.5–33.5°.

the first charge/discharge platform of NVPF-C and NVPF-CNB composites at 0.5C. NVPF-CNB-30 shows a maximum specific discharge capacity of 106 mA h g^{-1} at 0.5C. The specific discharge capacities of NVPF-C, NVPF-CNB-20, and NVPF-CNB-40 are 82, 100, and 99 mA h g^{-1}, respectively. Compared with NVPF-C, the NVPF-CNB composite exhibits a flatter platform and a smaller voltage difference, indicating the positive effect of N and B co-doping on the electrochemical performance. Fig. 7b shows that after 100 cycles at 0.5C, the capacity retention rates of NVPF-CNB-30, NVPF-CNB-20, NVPF-CNB-40, and NVPF-C are 98, 95, 96, and 89%, respectively. Clearly, composite NVPF-CNB shows excellent reversibility, mainly due to the stable CNB framework constructed by N and B co-doping in the carbon layer, facilitating the diffusion of sodium ions and providing more space for sodium storage. Moreover, Fig. 7d shows the rate performance of four materials. The discharge capacities of NVPF-CNB-30 composite at 0.1, 0.2, 0.5, 1, 5, 10, 15, and 20C are 111, 107, 104, 103, 97, 87, 67 and 55 mA h g^{-1}, respectively. When the rate returns to 0.1C, the discharge capacity returns to 110 mA h g^{-1}, showing excellent

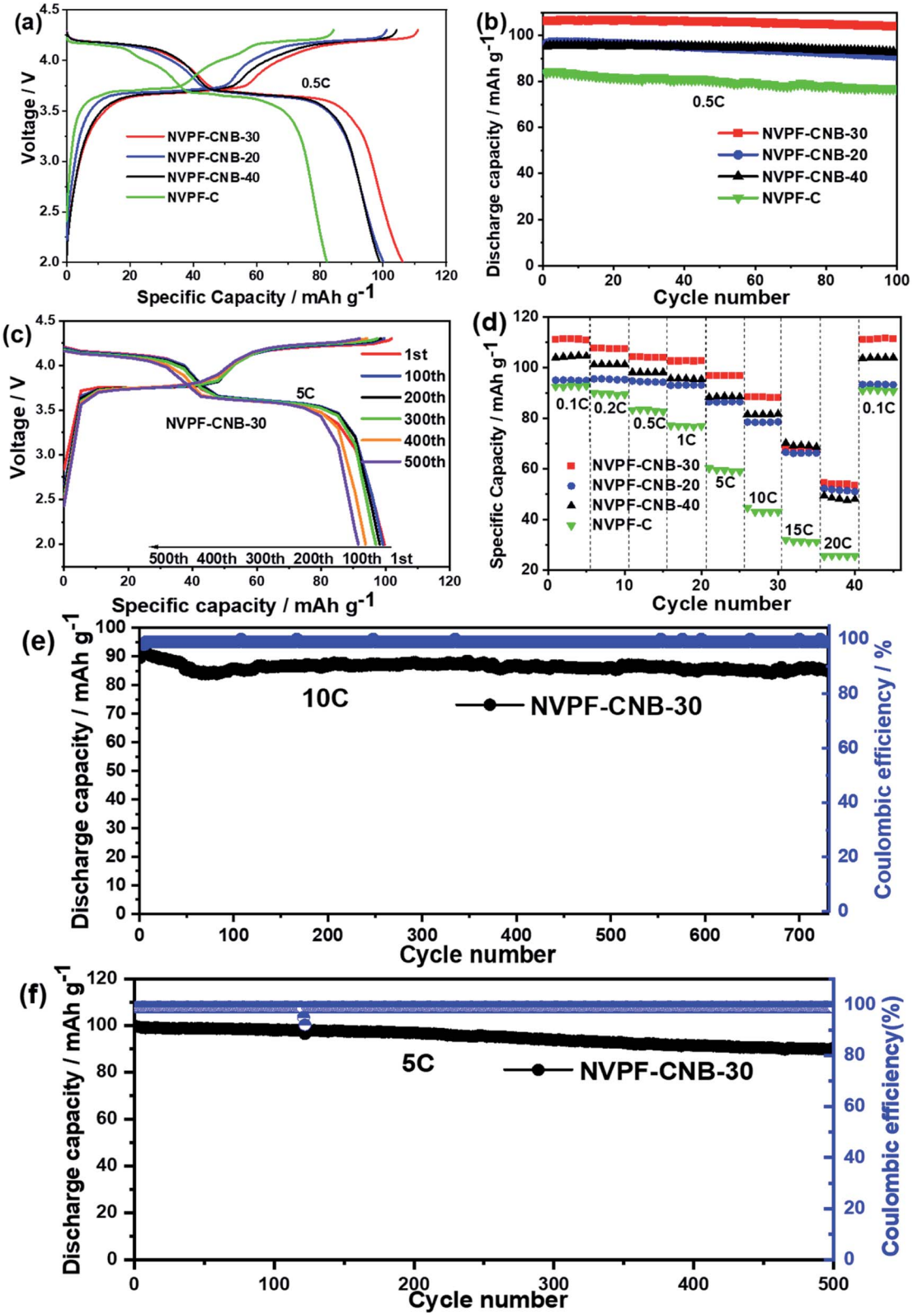

Fig. 7 (a) Initial charge/discharge profiles at 0.5C of all samples, (b) cycling performance at 0.5C of all samples, (c) the charge/discharge curves of NVPF-CNB-30 during the 1st, 100th, 200th, 300th, 400th, and 500th cycles at 5C, (d) rate performance at different rates for all samples, (e) long-term cycling stability of NVPF-CNB-30 at 10C, and (f) long-term cycling stability of NVPF-CNB-30 at 5C.

electrochemical reversibility and structural stability after the high-rate cycle. Fig. 7c shows the charge/discharge curves of NVPF-CNB-30 at the 1st, 100th, 200th, 300th, 400th, and 500th cycles at 5C. The electrode is affected by polarization under high-rate cycles; therefore, the NVPF charge/discharge curve plateau is still observed in cycles of different turns. To further illustrate the stability of the composite under high-rate cycling, the charge/discharge curves of the NVPF-CNB-30 composite at 5C and 10C, respectively, were obtained as shown in Fig. 7f and e. The initial reversible capacity is 99 and 90 mA h g^{-1}, the capacity retention rate after 500 cycles at 5C is 91.9%, while the capacity retention rate after 730 cycles at 10C is about 95.5%. The N and B co-doped carbon layer structure is more stable, prevents the material from corrosion, and improves the cyclic stability.

The dynamic properties of NVPF-CNB-30 composites were studied by CV at different scan rates in the range of 2.5–4.5 V. Fig. 8a shows that two pairs of redox peaks appear at 3.60/3.80 and 4.10/4.25 for the material. With increasing scanning rate, both oxidation and reduction peaks appear offset. Moreover, the oxidation and reduction peaks are symmetrical at different scanning rates, indicating the reversible deintercalation reaction of sodium ions. Fig. S4† shows the four-cycle CV curves of NVPF-CNB-30 composite and NVPF-C at a scanning rate of 0.4 mV s^{-1}. The CV of each cycle coincides, and the polarization voltage difference of the two pairs of oxidation/reduction peaks of NVPF-CNB-30 is 0.19 and 0.12 V, respectively, while for NVPF-C the values are 0.22 and 0.13 V, indicating that NVPF-CNB-30 possesses more electro-chemical reversibility with lower polarization. The sodium ion diffusion coefficient can be calculated at different peak positions by linear fitting the arithmetic square root of scanning velocity and peak current in the CV curve, according to the Randles–Sevcik equation (1). Fig. 8b shows that the slopes at A2/C2 are lower than those at A1/C1, respectively, thus the reaction kinetic performance of Na^+ is higher at 3.7 V. Table S1† lists the sodium ion diffusion coefficients at peak positions for all samples at a scan rate of 0.5 mV s^{-1}. The sodium ion diffusion coefficient values of NVPF-CNB-30 are 4.9 × 10^{-11} (A1), 3.5 × 10^{-11} (A2), 1.94 × 10^{-11} (C1) and 2.7 × 10^{-11} cm^2 s^{-1} (C2), much higher than those of NVPF-C. The high diffusion coefficient of NVPF-CNB-30 is mainly attributed to the synergistic effect between N and B in the carbon layer.[76] The electrochemical impedance tests on NVPF-C and NVPF-CNB composites are carried out and results are shown in Fig. 8c. All electrochemical impedance spectra are composed of a semicircle in the high-frequency region and a diagonal line in the low-frequency region. The semicircle in the high-frequency region represents the charge transfer impedance (R_{ct}), and the diagonal line in the low-frequency region represents the sodium diffusion process. Table 2 summarizes that NVPF-CNB-30 exhibits the smallest charge transfer resistance. To further illustrate the better dynamic performance of NVPF-CNB-30, the diffusion coefficient of sodium ions was calculated by applying the formulas (2) and (3). The Warburg impedance coefficient was obtained by plotting Z' and $\omega^{-1/2}$ (Fig. 8d). Table 1 presents that NVPF-CNB-30 shows the largest diffusion coefficient of sodium ions, attributed to the effective electronic conductive network formed by N and B co-

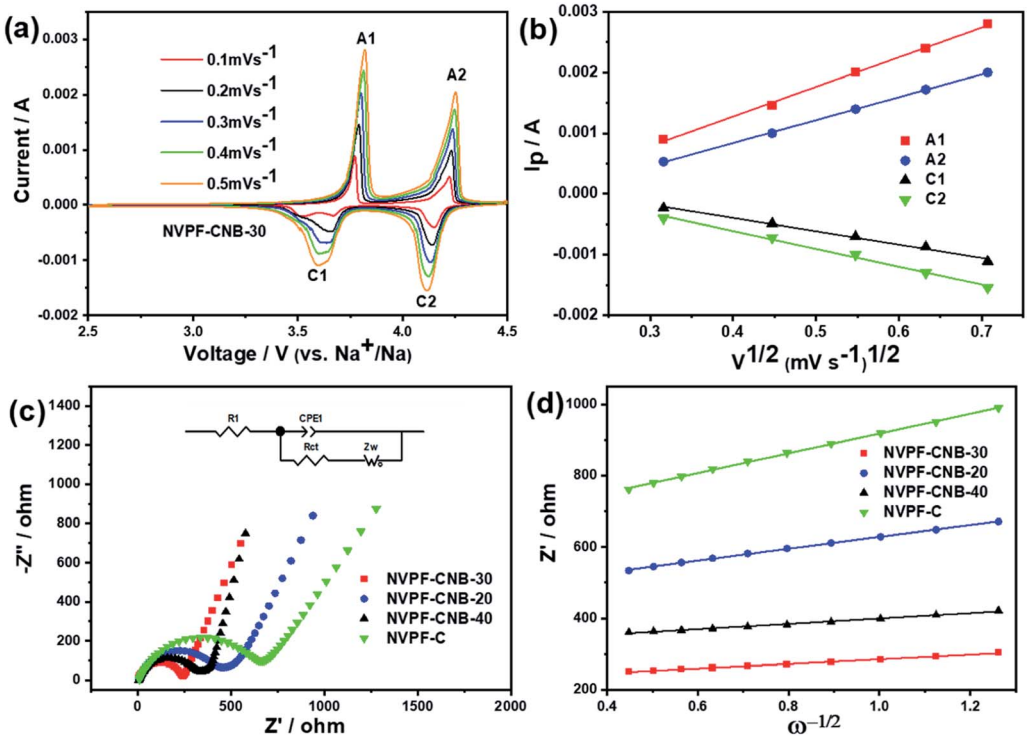

Fig. 8 (a) CV curves of NVPF-CNB-30 at various scan rates, (b) the linear relationship of I_p and $v^{1/2}$ for NVPF-CNB-30, (c) EIS curves of all samples, (d) relationship between Z' and $\omega^{-1/2}$ in the low-frequency region of all samples.

Table 1 Comparison of the electrochemical properties of NVPF cathode with previously reported electrodes used in sodium ion batteries

Electrode	Voltage window	Initial discharge capacity (mA h g^{-1})	Capacity retention ratio (%)	Reference
NVPF-CNB-30	2.5–4.5	111 (0.1C) 95 (5C)	98%, 95.5% (0.5C after 100 cycles and 10C after 730 cycles)	This study
NVPF	3.2–4.2	110 (0.1C)	95% (0.1C after 60 cycles)	69
NVPF	2.0–4.5	109 (0.1C)	96.3% (0.1C after 30 cycles)	70
NVPF	2.0–4.6	111 (0.091C)	93% (0.1C after 40 cycles)	71
NVPF	1.5–4.5	103 (0.2C)	91.5% (5C after 500 cycles)	72
NVPF	2.5–4.6	84 (2C)	99% (2C after 190 cycles)	73
NVPF@rGO	2.0–4.5	95 (2C)	87.5% (0.2C after 70 cycles)	74
NVPF-CNT	2.0–4.6	91 (4C)	99.4% (1C after 100 cycles)	75

Table 2 Charge transfer resistance and sodium ion diffusion coefficient of all samples

Sample	R_{ct} (Ω)	D_{Na^+} ($cm^2\ s^{-1}$)
NVPF-CNB-30	233	2.28×10^{-15}
NVPF-CNB-20	456	3.39×10^{-16}
NVPF-CNB-40	339	1.26×10^{-15}
NVPF-C	670	1.21×10^{-16}

doped carbon layer, which improves the diffusion of sodium ions.

$$I_p = 2.69 \times 10^5 n^{\frac{3}{2}} A D^{\frac{1}{2}} C_{Na} v^{\frac{1}{2}} \quad (1)$$

where I_p is the peak current of anodic and cathodic reaction, n is the number of electrons transfer during the electrochemical reaction, C denotes the concentration of sodium ions in the electrode, D represents the diffusion of sodium ions in the electrode, A is the area of the electrode, and v denotes the scan rate.

$$D = R^2T^2/2A^2n^4F^4C^2\sigma^2 \quad (2)$$

$$Z' = R_s + R_{ct} + \sigma_\omega \omega^{-\frac{1}{2}} \quad (3)$$

where R is the gas constant, T is the absolute temperature, A refers to the surface area, n is the number of electrons per molecule during the oxidation process, F denotes the Faraday constant, C is the concentration of sodium ions, and σ refers to Warburg impedance coefficient.

4. Conclusions

The N and B co-doped carbon layer NVPF composites were successfully synthesized by simple sol–gel method. The NVPF-CNB composite exhibits excellent electrochemical performance, in particular, the rate performance and cyclic stability. The initial capacity of the NVPF-CNB-30 composite is 99 and 90 mA h g^{-1} at 5C and 10C, respectively. The capacity retention rate is about 91.9% after 500 cycles at 5C, and 95.5% after 730 cycles at 10C. This is mainly attributed to the porous structure of NVPF-CNB and the N and B co-doping of the carbon layer. The porous structure facilitates the diffusion of sodium ions. The N and B co-doping of the carbon layer provides more active sites and builds a stable CNB framework, thus leading to the improvement in the electrochemical performance of the cathode material. *in situ* XRD analysis showed that the nitrogen and boron co-doped carbon-coated $Na_3V_2(PO_4)_2F_3$ exhibited good cycling reversibility. Using ionic liquid as a modification material to synthesize nitrogen and boron co-doped carbon-coated NVPF also provides more options for subsequent modification methods.

Conflicts of interest

There are no conflicts to declare.

Acknowledgements

This research was supported by the Guangdong Basic and Applied Basic Research Foundation (Grant No. 2022A1515011985), the Shenzhen Science and Technology Planning Project (Grant No. JCYJ20190808115609663 and JCYJ20190808123207674), and the Scientific Research Project of Guangdong Provincial Department of Education (Grant No. 2020ZDZX2040).

References

1 C. Delmas, *Adv. Energy Mater.*, 2018, **8**, 1703137.
2 H. Li, T. Jin, X. Chen, Y. Lai, Z. Zhang, W. Bao and L. Jiao, *Adv. Energy Mater.*, 2018, **8**, 1801418.
3 J. Y. Hwang, J. Kim, T. Y. Yu and Y. K. Sun, *Adv. Energy Mater.*, 2019, **9**, 1803346.
4 Z. Lv, M. Ling, M. Yue, X. Li, M. Song, Q. Zheng and H. Zhang, *J. Energy Chem.*, 2021, **55**, 361–390.
5 Z. Zhang, Z. Chen, Z. Mai, K. Peng, Q. Deng, A. Bayaguud, P. Zhao, Y. Fu, Y. Yu and C. Zhu, *Small*, 2019, **15**, 1900356.
6 J. Liao, C. Chen, Q. Hu, Y. Du, Y. He, Y. Xu, Z. Zhang and X. Zhou, *Angew. Chem., Int. Ed.*, 2021, **60**, 25575–25582.
7 Z. Zhang, Y. Du, Q. C. Wang, J. Xu, Y. N. Zhou, J. Bao, J. Shen and X. Zhou, *Angew. Chem., Int. Ed.*, 2020, **59**, 17504–17510.
8 Q. Zheng, H. Yi, X. Li and H. Zhang, *J. Energy Chem.*, 2018, **27**, 1597–1617.
9 J. Landesfeind, T. Hosaka, M. Graf, K. Kubota, S. Komaba and H. A. Gasteiger, *J. Electrochem. Soc.*, 2021, **168**, 40538.

10 J. Xu, J. Chen, L. Tao, Z. Tian, S. Zhou, N. Zhao and C. Wong, *Nano Energy*, 2019, **60**, 510–519.
11 W. X. Zhan, C. L. Fan, W. H. Zhang, G. D. Yi, H. Chen, S. C. Han and J. S. Liu, *Int. J. Energy Res.*, 2020, **44**, 6608–6622.
12 J. Pan, S. Chen, Q. Fu, Y. Sun, Y. Zhang, N. Lin, P. Gao, J. Yang and Y. Qian, *ACS Nano*, 2018, **12**, 12869–12878.
13 M. Luo, H. Yu, F. Hu, T. Liu, X. Cheng, R. Zheng, Y. Bai, M. Shui and J. Shu, *Chem. Eng. J.*, 2020, **380**, 122557.
14 Q. Zhao, F. K. Butt, Z. Guo, L. Wang, Y. Zhu, X. Xu, X. Ma and C. Cao, *Chem. Eng. J.*, 2021, **403**, 126308.
15 G. Du and H. Pang, *Energy Storage Mater.*, 2021, **36**, 387–408.
16 Z. Wang, Y. Huang, R. Luo, F. Wu, L. Li, M. Xie, J. Huang and R. Chen, *J. Power Sources*, 2019, **436**, 226868.
17 I. Shakhova, M. G. Rozova, D. Burova, D. S. Filimonov, O. A. Drozhzhin and A. M. Abakumov, *J. Solid State Chem.*, 2020, **281**, 121010.
18 D. Semykina, O. Podgornova and N. Kosova, *Mater. Today: Proc.*, 2020, **25**, 497–500.
19 P. N. Didwal, R. Verma, C. Min and C. Park, *J. Power Sources*, 2019, **413**, 1–10.
20 J. Ou, L. Yang, F. Jin, S. Wu and J. Wang, *Adv. Powder Technol.*, 2020, **31**, 1220–1228.
21 Y. Fang, J. Zhang, L. Xiao, X. Ai, Y. Cao and H. Yang, *Adv. Sci.*, 2017, **4**, 1600392.
22 E. Gu, S. Liu, Z. Zhang, Y. Fang, X. Zhou and J. Bao, *J. Alloys Compd.*, 2018, **767**, 131–140.
23 E. Gu, J. Xu, Y. Du, X. Ge, X. Zhu, J. Bao and X. Zhou, *J. Alloys Compd.*, 2019, **788**, 240–247.
24 J. Xu, E. Gu, Z. Zhang, Z. Xu, Y. Xu, Y. Du, X. Zhu and X. Zhou, *J. Colloid Interface Sci.*, 2020, **567**, 84–91.
25 A. Mukherjee, T. Sharabani, I. Perelshtein and M. Noked, *Batteries Supercaps*, 2020, **3**, 52–55.
26 J. Cheng, Y. Chen, S. Sun, Z. Tian, Y. Linghu, Z. Tian, C. Wang, Z. He and L. Guo, *Ceram. Int.*, 2021, **47**, 18065–18074.
27 Y. Qi, Z. Tong, J. Zhao, L. Ma, T. Wu, H. Liu, C. Yang, J. Lu and Y. Hu, *Joule*, 2018, **2**, 2348–2363.
28 J. Xu, J. Chen, L. Tao, Z. Tian, S. Zhou, N. Zhao and C. Wong, *Nano Energy*, 2019, **60**, 510–519.
29 L. Li, Y. Xu, X. Sun, S. He and L. Li, *Chem. Eng. J.*, 2018, **331**, 712–719.
30 L. Zhao, H. Zhao, X. Long, Z. Li and Z. Du, *ACS Appl. Mater. Interfaces*, 2018, **10**, 35963–35971.
31 Y. Cai, X. Cao, Z. Luo, G. Fang, F. Liu, J. Zhou, A. Pan and S. Liang, *Adv. Sci.*, 2018, **5**, 1800680.
32 J. Cheng, Y. Chen, S. Sun, Z. Tian, Y. Linghu, Z. Tian, C. Wang, Z. He and L. Guo, *Ceram. Int.*, 2021, **47**, 18065–18074.
33 Y. Li, X. Liang, G. Zhong, C. Wang, S. Wu, K. Xu and C. Yang, *ACS Appl. Mater. Interfaces*, 2020, **12**, 25920–25929.
34 J. Zhao, X. Yang, Y. Zhang, X. J. Loh, X. Hu, G. Chen, F. Du and Q. Yan, *J. Mater. Chem. A*, 2019, **7**, 1548–1555.
35 C. Wang, D. Du, M. Song, Y. Wang and F. Li, *Adv. Energy Mater.*, 2019, **9**, 1900022.
36 Y. Xiao, P. Wang, Y. Yin, Y. Zhu, Y. Niu, X. Zhang, J. Zhang, X. Yu, X. Guo, B. Zhong and Y. Guo, *Adv. Mater.*, 2018, **30**, 1803765.
37 X. Cao, A. Pan, B. Yin, G. Fang, Y. Wang, X. Kong, T. Zhu, J. Zhou, G. Cao and S. Liang, *Nano Energy*, 2019, **60**, 312–323.
38 X. Yang, X. Wang and W. Zhen, *Ceram. Int.*, 2020, **46**, 9170–9175.
39 K. Sun, Y. Hu, X. Zhang, K. San Hui, K. Zhang, G. Xu, J. Ma and W. He, *Electrochim. Acta*, 2020, **335**, 135680.
40 H. Xiao, X. Huang, Y. Ren, H. Wang, J. Ding, S. Zhou, X. Ding and Y. Chen, *J. Alloys Compd.*, 2018, **732**, 454–459.
41 Y. Li, X. Liang, G. Zhong, C. Wang, S. Wu, K. Xu and C. Yang, *ACS Appl. Mater. Interfaces*, 2020, **12**, 25920–25929.
42 X. Huang, X. Yi, Q. Yang, Z. Guo, Y. Ren and X. Zeng, *Ceram. Int.*, 2020, **46**, 28084–28090.
43 Y. Zhu, K. Song, S. Shen, Z. Liu, J. Xu, L. Yang and L. Zhao, *J. Alloys Compd.*, 2021, **856**, 157992.
44 X. Huang, X. Yi, Q. Yang, Z. Guo, Y. Ren and X. Zeng, *Ceram. Int.*, 2020, **46**, 28084–28090.
45 Q. Wang, Q. Wang, M. Zhang, B. Han, C. Zhou, Y. Chen and G. Lv, *J. Mol. Model.*, 2019, **25**, 96.
46 Y. Jiang, X. Zhou, D. Li, X. Cheng, F. Liu and Y. Yu, *Adv. Energy Mater.*, 2018, **8**, 1800068.
47 M. Moradi, M. Nangir and A. Massoudi, *Appl. Surf. Sci.*, 2021, **562**, 150156.
48 A. Balducci, *Top. Curr. Chem.*, 2017, **375**, 20.
49 M. Benchakar, R. Naéjus, C. Damas and J. Santos-Peña, *Electrochim. Acta*, 2020, **330**, 135193.
50 H. Niu, L. Wang, P. Guan, N. Zhang, C. Yan, M. Ding, X. Guo, T. Huang and X. Hu, *J. Energy Storage*, 2021, **40**, 102659.
51 M. Duan, F. Zhu, G. Zhao, J. Hu, H. Zhang, G. Ren, Y. Meng and Z. Fan, *Microporous Mesoporous Mater.*, 2020, **306**, 110433.
52 X. Xu, L. Si, X. Zhou, F. Tu, X. Zhu and J. Bao, *J. Power Sources*, 2017, **349**, 37–44.
53 Z. Zhao, H. Li, Z. Yang, S. Hao, X. Wang and Y. Wu, *J. Alloys Compd.*, 2020, **817**, 152751.
54 L. Li, Y. Xu, X. Sun, S. He and L. Li, *Chem. Eng. J.*, 2018, **331**, 712–719.
55 S. Park, J. Song, S. Kim, B. Sambandam, V. Mathew, S. Kim, J. Jo, S. Kim and J. Kim, *Nano Res.*, 2019, **12**, 911–917.
56 L. Zheng, Y. Xue, L. Deng, G. Wu, S. Hao and Z. Wang, *Ceram. Int.*, 2019, **45**, 4637–4644.
57 Y. Zhu, K. Song, S. Shen, Z. Liu, J. Xu, L. Yang and L. Zhao, *J. Alloys Compd.*, 2021, **856**, 157992.
58 L. Deng, G. Sun, K. Goh, L. Zheng, F. Yu, X. Sui, L. Zhao and Z. Wang, *Electrochim. Acta*, 2019, **298**, 459–467.
59 Q. Liu, D. Wang, X. Yang, N. Chen, C. Wang, X. Bie, Y. Wei, G. Chen and F. Du, *J. Mater. Chem. A*, 2015, **3**, 21478–21485.
60 A. Mukherjee, T. Sharabani, R. Sharma, S. Okashy and M. Noked, *Batteries Supercaps*, 2020, **3**, 510–518.
61 L. Hu, S. Cheng, S. Xiao, W. Li, Z. Chen, W. Li, B. Huang, Q. Liu and Q. Chen, *ChemElectroChem*, 2020, **7**, 3975–3983.
62 M. Ling, F. Li, H. Yi, X. Li, G. Hou, Q. Zheng and H. Zhang, *J. Mater. Chem. A*, 2018, **6**, 24201–24209.
63 S. Xu, H. Li and X. Wang, *ChemElectroChem*, 2021, **8**, 866–872.

64 P. Tao, J. He, T. Shen, Y. Hao, J. Yan, Z. Huang, X. Xu, M. Li and Y. Chen, *Adv. Mater. Interfaces*, 2019, **6**, 1900460.
65 L. Zhang, G. Xia, Z. Guo, X. Li, D. Sun and X. Yu, *Int. J. Hydrogen Energy*, 2016, **41**, 14252–14260.
66 Y. Jiang, X. Zhou, D. Li, X. Cheng, F. Liu and Y. Yu, *Adv. Energy Mater.*, 2018, **8**, 1800068.
67 J. Guo, P. Wang, X. Wu, X. Zhang, Q. Yan, H. Chen, J. Zhang and Y. Guo, *Adv. Mater.*, 2017, **29**, 1701968.
68 M. Bianchini, F. Fauth, N. Brisset, F. Weill, E. Suard, C. Masquelier and L. Croguennec, *Chem. Mater.*, 2015, **27**, 3009–3020.
69 N. Pianta, D. Locatelli and R. Ruffo, *Ionics*, 2021, **27**, 1853–1860.
70 R. A. Shakoor, D. Seo, H. Kim, Y. Park, J. Kim, S. Kim, H. Gwon, S. Lee and K. Kang, *J. Mater. Chem.*, 2012, **22**, 20535.
71 W. Song, Z. Wu, J. Chen, Q. Lan, Y. Zhu, Y. Yang, C. Pan, H. Hou, M. Jing and X. Ji, *Electrochim. Acta*, 2014, **146**, 142–150.
72 M. Wang, X. Huang, H. Wang, T. Zhou, H. Xie and Y. Ren, *RSC Adv.*, 2019, **9**, 30628–30636.
73 W. Song, X. Ji, Z. Wu, Y. Zhu, F. Li, Q. Yao and C. E. Banks, *RSC Adv.*, 2014, **4**, 11375–11383.
74 P. Du, K. Mi, F. Hu, X. Jiang, D. Wang and X. Zheng, *New J. Chem.*, 2020, **44**, 12985–12992.
75 N. Eshraghi, S. Caes, A. Mahmoud, R. Cloots, B. Vertruyen and F. Boschini, *Electrochim. Acta*, 2017, **228**, 319–324.
76 B. Ren, W. Li, A. Wei, X. Bai, L. Zhang and Z. Liu, *J. Alloys Compd.*, 2018, **740**, 784–789.